ISSN: 2994-6433

Research Article

Journal of Sensor Networks and Data Communications

First-Principles Modeling of Electro-Thermal Surface Interactions in Pulsed CCFL-Backlit Displays

Ahmed M. Hala*

Gaseous electronics LLC Riyadh, Saudi Arabia

***Corresponding Author**
Ahmed M. Hala, Gaseous electronics LLC Riyadh, Saudi Arabia.

Submitted: 2026, May 05; **Accepted:** 2026, Jun 26; **Published:** 2026, Sep 15

Citation: Hala, A. M. (2026). First-Principles Modeling of Electro-Thermal Surface Interactions in Pulsed CCFL-Backlit Displays. *J Sen Net Data Comm, 6*(3), 01-18.

Abstract

This paper presents a first-principles physical model to investigate the influence of cold cathode fluorescent lamp (CCFL) backlighting on the behavior of surface species at the liquid crystal display (LCD) interface. While CCFL technology is primarily optimized for optical throughput, its high-voltage (500–1500 Vrms), high-frequency (20–80 kHz) AC drive generates fringe electric fields and thermal gradients that penetrate the multi-layered LCD dielectric stack. We utilize a multiphysics framework to quantify the forces acting on water nanofilms, atmospheric ions, neutral volatile organic compounds (VOCs), and micron-scale dust particles. By applying a quasi-static approximation of Maxwell's equations alongside Arrhenius-based desorption kinetics, we demonstrate that the display acts as an electro-thermal actuator. Analytical results and 2.5D finite element simulations reveal that electrostatic forces (10^{-15}–10^{-12} N) dominate gravitational effects for sub-micron particles, below a charge- and field-dependent crossover radius $r_c \approx 0.3$–1.3 μm, facilitating "dust banding" through geometric field enhancement at bezel boundaries. We further show that at 20–80 kHz the oscillatory movement of a charged particle is of nanometer scale, so that dust responds only to the cycle-averaged dielectrophoretic force while small ions, being far more mobile, do track the instantaneous field — a separation that accounts for the distinct spatial signatures of ionic and particulate contamination. We show that the pulsed nature of the backlight drive, controlled by Pulse Width Modulation (PWM), produces a nonlinear enhancement of thermally activated desorption because the Arrhenius desorption rate responds nonlinearly to the periodically varying surface temperature. This effect modifies the balance between thermal desorption and electrically mediated surface transport. The paper's numerical findings establish that the CCFL backlight is not a passive illuminator but an active electro-thermal actuator whose fringe fields (10^3–10^5 Vm^{-1}), thermal gradients (10–20◦C), and dielectrophoretic particle capture (forces of 10^{-12} N) all couple into the optical path of the LCD. For a satellite-broadcast video stream, these mechanisms impose a spatially non-uniform, time-varying distortion on the rendered content — LC director perturbation at the bezel, thermal gamma modulation at the PWM frequency, and progressive contrast degradation from particle accumulation — that is inseparable from the display's own operation and therefore indistinguishable from a source-level artifact by the receiver.

Keywords: CCFL Backlighting, LCD Surface Physics, Electro-Thermal Transport, Fringe Electric Fields, Dust Deposition, Particle Kinetics, Multiphysics Modeling, Surface Contamination

1. Introduction

The interaction between Cold Cathode Fluorescent Lamp (CCFL) backlights and the external environment of a Liquid Crystal Display (LCD) constitutes a complex multiphysics problem at the intersection of electrostatics, thermodynamics, surface science, and aerosol dynamics. While the primary function of the CCFL is to provide uniform illumination through the diffuser stack, its high-voltage alternating current (AC) drive (typically 500–1500 V_{rms} at 20–80 kHz) generates significant fringe electric fields that penetrate the multi-layered dielectric stack of the display [1-3,10,9]. These fringe fields, combined with the thermal gradients induced by the CCFL tubes, actively influence the behavior of surface-adsorbed species—including water nanofilms, atmospheric ions, volatile organic compounds (VOCs), and micron-scale dust particles. Conventional optical-focused treatments of LCDs have largely overlooked these secondary electro-thermal effects [1]. Recent studies, however, have begun to document non-random contamination patterns such as "dust banding," "ionic spotting," and surface haze on legacy CCFL-backlit displays, phenomena that cannot be explained by gravitational settling or simple diffusion alone [5,25].

This paper establishes a comprehensive first-principles framework to quantify these inter-actions. We derive the effective surface electric field E_s through a rigorous capacitive voltage divider analysis across the layered dielectric stack, incorporating partial ITO shielding and geometric field enhancement at the bezel edges [6,22]. A nonlinear thermal pumping mechanism under Pulse Width Modulation (PWM) is proven using second-order Taylor expansion of the Arrhenius desorption rate about the cycle-averaged temperature, together with the temporal asymmetry between electrical and thermal timescales. Furthermore, we establish the regime boundary at which electrostatic forces cease to dominate gravity, through direct force-ratio calculations and an analysis of AC-induced oscillatory motion that retains both inertia and Stokes drag [13,5,19]. The model integrates quasi-static Maxwell equations, Arrhenius-based desorption kinetics, dielectrophoretic particle transport, and Lagrangian tracking within a 2.5D finite-element framework [4,6,11,12,14,24]. By coupling these physical domains, we show that the CCFL-backlit LCD functions as a weak but persistent electro-thermal actuator, producing spatially modulated contamination patterns that are particularly pronounced at bezel perimeters and lamp-end regions.

This theoretical foundation not only explains empirically observed degradation mechanisms in industrial, military, and medical LCD hardware but also provides predictive tools for maintenance and improved contamination-resistant designs in legacy systems. The remainder of the paper details the theoretical derivations, (Section 2), methodology (Section 3), multiphysics simulations and discussion (Section 4), and practical implications (Section 5).

2. Theoretical Framework

This section presents the core first-principles derivations that form the foundation of the proposed electro-thermal model. Building upon the multiphysics nature of the CCFL-LCD system outlined in Section 1, we develop three key theoretical results. First, we derive the effective surface electric field by accounting for the layered dielectric structure, the finite sheet resistance of the ITO electrodes, and geometric field enhancement at the display boundaries. Second, we derive the nonlinear enhancement of thermally activated desorption under PWM operation, showing how the convex temperature dependence of the Arrhenius desorption rate causes the cycle-averaged desorption rate to exceed that of an isothermal surface maintained at the same mean temperature. Third, we establish the particle-size regime in which electrostatic forces can exceed gravitational settling and characterize the corresponding frequency-dependent particle response when both inertia and Stokes drag are retained. These derivations provide the analytical backbone for the methodology, species-specific mechanisms, and multiphysics simulations presented later in the paper.

Convention. Throughout this paper r and a denote particle radius. Where a source or figure quotes a particle diameter, the corresponding radius is given explicitly.

2.1. Effective Surface Electric Field in a Multi-Layer Dielectric Stack with Partial ITO Shielding

The outer-surface field E_s is not a simple uniform divider because of the finite conductivity of the ITO layers and the presence of fringe leakage at the boundaries. We derive the effective transmission factor rigorously.

Consider the LCD stack as N dielectric slabs in series between the CCFL high-voltage electrode (potential $V(t) = V_0 \sin(\omega t)$) and the outer polarizer surface. In the quasi-static regime ($\omega \ll c/L$, where L is the lateral dimension of the display), the displacement field $\mathbf{D}$ is divergence-free in the absence of free charge ($\nabla \cdot \mathbf{D} = 0$).
For planar layers the potential drop satisfies:

$$V_L = \sum_{i=1}^{N} E_i \, d_i = \sum_{i=1}^{N} \frac{D}{\epsilon_0 \, \epsilon_{r,i}} \, d_i. \tag{1}$$

Thus,

$$D = \frac{\epsilon_0 \, V_L}{\sum_i (d_i/\epsilon_{r,i})}. \tag{2}$$

The electric field in the outermost layer (polarizer, $\epsilon_{r,s}$) is therefore

$$E_s = \frac{D}{\epsilon_0 \, \epsilon_{r,s}} = \frac{V_L}{\epsilon_{r,s} \sum_i (d_i/\epsilon_{r,i})}, \tag{3}$$

which expresses the effective transmission of the stack; for compactness we write $\varepsilon_{\text{eff}} \equiv \varepsilon_{r,s}$ in what follows.

Correction for partial ITO shielding and fringe leakage. The ITO layers have finite sheet resistance ($R_s \approx 10{-}100\ \Omega/\square$) and therefore

cannot be treated as perfect equipotentials at high frequency. We model each ITO layer as a thin transition boundary characterized by the corresponding sheet conductance $G_s = 1/R_s$, with tangential surface current density given by $\mathbf{J}_s = G_s\mathbf{E}\|$. This finite lateral conductance permits a non-zero tangential field near the termination of the ITO layer and contributes to the leakage of the electric field into the surrounding dielectric and air.

Solving the boundary-value problem (via separation of variables or conformal mapping near the bezel edge) yields a geometric field-enhancement factor $\xi(x)$ such that

$$E_{\text{edge}}(x) \approx \xi(x)\, E_s^{\text{center}}, \qquad \xi \in [5,\, 10] \tag{4}$$

near the bezel–glass–air triple line, where x is measured inward from the ITO termination. The enhancement originates from the dielectric mismatch and the abrupt termination of the conductive plane.

A full 2.5D finite-element solution (see Section 4) reproduces the predicted boundary-field enhancement for the modeled geometry. An analytical approximation using the method of images for a semi-infinite grounded plane gives

$$\xi \approx 1 + \frac{2}{\pi} \ln\left(\frac{h}{r_{\text{edge}}}\right), \tag{5}$$

where h is the distance from the ITO edge to the observation point and r_{edge} is the effective corner radius. This field crowding directly explains the strong "dust banding" observed empirically at the display perimeter.

2.2 Nonlinear Enhancement of VOC Desorption under PWM Drive

The CCFL backlight is operated with a periodic PWM modulation that produces a timedependent thermal input to the display stack. Because the thermal response of the glass and polarizer layers is much slower than the electrical modulation, the surface temperature does not instantaneously reproduce the electrical PWM waveform. For the analytical desorption calculation, the resulting periodic surface-temperature excursion is represented by the simplified waveform

$$T(t) = T_0 + \Delta T\, \Pi_{\text{duty}}(t), \tag{6}$$

where T_0 is the baseline surface temperature, ΔT is the temperature excursion associated with the modulated heating, and $\Pi_{\text{duty}}(t)$ is a periodic rectangular function with modulation frequency f_m = 100–1000 Hz and duty cycle D. Under this representation, the cycle-averaged temperature is

$$\langle T \rangle = T_0 + D\, \Delta T. \tag{7}$$

Equation (6) is therefore used as an analytical representation of the periodic thermal state for evaluating the nonlinear desorption response; it is not intended to imply that the physical surface temperature changes instantaneously with the electrical PWM waveform. In practice, the finite thermal time constant of the display stack ($\tau_{\text{th}} \approx 0.1$–$1$ s) low-pass filters the PWM-induced heat input, so the actual surface-temperature modulation is smoother than the rectangular waveform of (6). The rectangular representation is retained here as a tractable analytical approximation; when quantitative accuracy is required, the full filtered thermal response should be used in place of (6).

The instantaneous thermally activated desorption rate is represented by the Arrhenius relation

$$k_{\text{des}}(T) = \nu \exp\left(-\frac{E_a}{R\,T(t)}\right), \tag{8}$$

where v is the attempt frequency, E_a is the activation energy for desorption, R is the molar gas constant, and $T(t)$ is the time-dependent surface temperature.

To describe the evolution of the adsorbed surface coverage θ, a Langmuir-type adsorption–desorption balance is used:

$$\frac{d\theta}{dt} = k_{\text{ads}}(T(t))\,(1-\theta) - k_{\text{des}}(T(t))\,\theta. \tag{9}$$

Here, k_{ads} represents the effective adsorption rate and k_{ads} is the temperature-dependent desorption rate given by (8). The change in

surface coverage over one PWM period, $\tau = 1/f_m$, is obtained by integrating (9) over that period.

Enhancement of cycle-averaged desorption. The desorption rate in (8) has a strongly nonlinear temperature dependence over the operating range considered here. For the Arrhenius form in (8), the second derivative with respect to temperature is positive when

$$T < \frac{E_a}{2R}. \tag{10}$$

For E_a = 40–80 kJ mol^{-1}, the corresponding upper temperature scale is approximately 2.4 – 4.8×10^3 K, which is far above the surface temperatures considered for the polarizer. The Arrhenius desorption rate is therefore convex over the relevant operating range. Jensen's inequality consequently gives

$$\langle k_{\mathrm{des}}(T)\rangle > k_{\mathrm{des}}(\langle T\rangle), \tag{11}$$

for a non-zero temperature modulation about a fixed mean temperature. Equation (11) establishes that periodic temperature modulation increases the cycle-averaged thermally activated desorption rate relative to an isothermal surface maintained at the same mean temperature. It does not, by itself, establish a net outward mass flux or a reduction in steady-state surface coverage, because those quantities additionally depend on adsorption kinetics and gas-phase transport through (9).

The magnitude of the nonlinear enhancement can be estimated by defining the temperature excursion about the cycle mean as

$$\delta T(t) = T(t) - \langle T\rangle. \tag{12}$$

For temperature excursions sufficiently small compared with the mean temperature, the Arrhenius rate can be expanded about $\langle T\rangle$ as

$$k_{\mathrm{des}}(T) \approx k_0 \left[1 + \frac{E_a}{R\langle T\rangle^2}\,\delta T + \frac{1}{2}\left(\left(\frac{E_a}{R\langle T\rangle^2}\right)^2 - \frac{2\,E_a}{R\langle T\rangle^3}\right)(\delta T)^2 + \cdots\right], \tag{13}$$

where

$$k_0 = k_{\mathrm{des}}(\langle T\rangle). \tag{14}$$

The second-order coefficient in (13) contains two terms: the squared first-derivative contribution $(E_a/(R\langle T\rangle^2))^2$ and a second-derivative correction $-2E_a/(R\langle T\rangle^3)$ arising from the curvature of $-E_a/(RT)$. Both terms are retained here for a consistent second-order expansion.

Averaging (13) over one PWM cycle eliminates the first-order term because $\langle \delta T\rangle = 0$. The leading nonlinear correction is therefore

$$\langle k_{\mathrm{des}}\rangle \approx k_0 \left[1 + \frac{1}{2}\left(\left(\frac{E_a}{R\langle T\rangle^2}\right)^2 - \frac{2\,E_a}{R\langle T\rangle^3}\right)\langle(\delta T)^2\rangle\right]. \tag{15}$$

For the rectangular PWM waveform defined in (6), the temperature variance about the cycle mean is

$$\langle(\delta T)^2\rangle = D(1-D)\,\Delta T^2. \tag{16}$$

Substitution of (16) into (15) gives the explicit second-order estimate

$$\langle k_{\mathrm{des}}\rangle \approx k_0 \left[1 + \frac{1}{2}\left(\left(\frac{E_a}{R\langle T\rangle^2}\right)^2 - \frac{2\,E_a}{R\langle T\rangle^3}\right)D(1-D)\,\Delta T^2\right]. \tag{17}$$

The positive second-order term in (17) is the quantitative manifestation of the convexity expressed by (11). For representative values E_a ≈ 40–80 kJ mol^{-1}, ΔT ≈ 10–20 ◦C, D = 0.5, and T_0 = 298 K, the second-order approximation predicts an increase in the cycle-averaged desorption rate of approximately 3–48% relative to an isothermal surface maintained at the same mean temperature. At the upper end of this parameter range, the expansion parameter becomes sufficiently large that the second-order truncation is no longer quantitatively reliable. Accordingly, (9) should be evaluated by direct numerical integration when the temperature excursion is sufficiently large for higher-order terms to become important.

The electrical and thermal responses also occur on different characteristic timescales. The CCFL electrical drive operates at 20–80 kHz, while the PWM modulation occurs at 100–1000 Hz and the thermal time constant of the display stack is approximately $\tau_{th} \approx 0.1$–1 s. Consequently, the electrical field can vary substantially while the surface temperature evolves more slowly. Charged species and polarizable particles can therefore respond to the rapidly varying electricfield environment, whereas the thermal state of the surface persists over a substantially longer interval. This temporal separation can modify the cycle-averaged balance between electrically mediated transport and thermally activated desorption [27].

Numerical integration of (9) over successive PWM cycles, using (6) and (8), with representative parameters $\nu \approx 10^{13}$ s^{-1}, E_a = 60 kJ mol^{-1}, $k_{ads} \approx 10^{-3}$ s^{-1}, D = 0.5, ΔT = 15 ◦C, and T_0 = 298 K, predicts a steady-state reduction in the modeled surface coverage θ of approximately 30–70% relative to a constant-temperature reference case maintained at the same mean surface temperature. This result is a model prediction under the specified adsorption, desorption, and thermal parameters and should not be interpreted as an experimentally measured reduction.

2.3 Electrostatic Dominance over Gravity: The Regime Boundary

For a spherical particle of radius r, density ρ, and charge q in a local electric field of magnitude E_s, the magnitude of the electrostatic force is

$$F_E = |q|\, E_s, \tag{18}$$

whereas the gravitational force is

$$F_g = \frac{4}{3}\pi r^3 \rho\, g. \tag{19}$$

The ratio of the two forces is therefore

$$\frac{F_E}{F_g} = \frac{|q|\, E_s}{\frac{4}{3}\pi r^3 \rho\, g}. \tag{20}$$

The crossover radius r_c at which electrostatic and gravitational forces have equal magnitude, $F_E = F_g$, follows directly from (20):

$$r_c = \left(\frac{3\,|q|\, E_s}{4\pi\rho\, g}\right)^{1/3}. \tag{21}$$

Using the representative parameter range $E_s \sim 10^3$–10^4 Vm^{-1}, $|q| \sim$ 10–100 e for triboelectrically charged dust [19,20], and $\rho \approx 2000$ kgm^{-3}, Eq. (21) gives

$$r_c \approx 0.3\,\mu\mathrm{m} \qquad (q = 10\,e,\ E_s = 10^3\,\mathrm{V\,m^{-1}}), \tag{22}$$

$$r_c \approx 0.6\,\mu\mathrm{m} \qquad (q = 100\,e,\ E_s = 10^3\,\mathrm{V\,m^{-1}}), \tag{23}$$

and

$$r_c \approx 1.3\,\mu\mathrm{m} \qquad (q = 100\,e,\ E_s = 10^4\,\mathrm{V\,m^{-1}}). \tag{24}$$

Thus, for the charge and field ranges considered here,

$$0.3\,\mu\mathrm{m} \lesssim r_c \lesssim 1.3\,\mu\mathrm{m}. \tag{25}$$

For $r \ll r_c$, Eq. (20) gives $F_E / F_g \gg 1$, so electrostatic forces can exceed gravitational settling by one or more orders of magnitude. Conversely, for $r \gg r_c$, the r^3 dependence of the gravitational force causes F_E / F_g to decrease rapidly and gravitational settling becomes increasingly important. The electrostatic-dominance regime is therefore primarily a sub-micron regime and should not be interpreted as applying uniformly to all particles below 10 μm.

The charge values used above represent a parameterization of triboelectrically charged particles rather than a universal charging law. In particular, field-charging saturation can yield substantially smaller charges for sub-micron particles. For example, the Pauthenier charging limit at $E_s = 10^4$ Vm^{-1} gives only approximately 3 e for a 0.5 μm particle. The crossover radius in (21) should therefore be

interpreted as charge- and field-dependent rather than as a single intrinsic particle-size threshold.

AC response of charged particles. In the 20–80 kHz CCFL drive field, a charged particle is subject to both inertia and viscous drag. For a sinusoidal electric field

$$E(t) = E_0 \cos(\omega t), \tag{26}$$

the steady-state displacement amplitude is

$$A = \frac{|q|\, E_0}{\omega \sqrt{(m\omega)^2 + \gamma^2}}, \qquad \gamma = \frac{6\pi \mu\, r}{C_c}, \qquad m = \frac{4}{3}\pi r^3 \rho, \tag{27}$$

where μ is the dynamic viscosity of air, C_c is the Cunningham slip correction, m is the particle mass, γ is the viscous drag coefficient, and $\omega = 2\pi f$ is the angular frequency of the applied field.

The corresponding particle relaxation time is

$$\tau_p = \frac{m}{\gamma}. \tag{28}$$

The purely inertial approximation,

$$A_{\text{inertial}} = \frac{|q|\, E_0}{m\, \omega^2}, \tag{29}$$

is recovered only when

$$\omega\, \tau_p \gg 1. \tag{30}$$

This condition is not satisfied throughout the sub-micron regime of interest. For example, at $f = 40$ kHz, the present model gives $\omega\tau_p \approx 0.12$ for $r = 0.1$ μm and $\omega\tau_p \approx 1.8$ for $r = 0.5$ μm. The viscous-drag term in (27) must therefore be retained when evaluating the particle response over the range considered here.

Evaluating (27) at $f = 40$ kHz, $q = 100\ e$, $E_0 = 10^4$ Vm^{-1}, and $\rho = 2000$ kgm^{-3} gives the oscillatory displacement amplitudes listed in Table 1.

r (μm)	$\omega\tau_p$	A (nm)	A/r
0.1	0.12	35	3.5×10^{-1}
0.5	1.8	2.1	4.2×10^{-3}
1.0	6.7	0.30	3.0×10^{-4}
2.5	39.9	0.019	7.8×10^{-6}
5.0	156.9	0.002	4.8×10^{-7}

Table 1: Oscillatory Displacement Amplitude Calculated from (27) at $f = 40$ kHz, $q = 100\ e$, $E_0 = 10^4$ Vm^{-1}, and $\rho = 2000$ kgm^{-3}.

Even at the full bezel enhancement represented by (4), corresponding to $\xi = 10$ and $E_0 = 10^5$ Vm^{-1}, the calculated excursion is approximately 0.35 μm for $r = 0.1$ μm and approximately 21nm for $r = 0.5$ µm. For particles with larger radii, the oscillatory displacement is substantially smaller than the particle diameter. These results indicate that micron-scale particles cannot undergo appreciable mechanical oscillation at the instantaneous 20–80 kHz field under the modeled conditions. Their net transport is instead expected to be governed primarily by the cycle-averaged dielectrophoretic force, together with gravitational, adhesive, and diffusive transport mechanisms [11,13,15,21].

The relevant cycle-averaged dielectrophoretic force for a polarizable particle is proportional to the spatial gradient of the squared electric field magnitude,

$$\langle \mathbf{F}_{\mathrm{DEP}} \rangle \propto \nabla \langle |\mathbf{E}|^2 \rangle. \tag{31}$$

Because this force depends on the field intensity rather than directly on the instantaneous field polarity, its cycle-averaged contribution can remain non-zero under an AC excitation. The 20–80 kHz drive therefore produces a strongly damped particle response rather than large periodic mechanical displacement.

Small atmospheric ions occupy a different dynamical regime because of their much higher electrical mobility. Using a representative ion mobility of $\mu_{\mathrm{ion}} \approx 1.5 \times 10^{-4}$ m^2 V^{-1} s^{-1}, the characteristic displacement associated with an oscillatory field is

$$A_{\mathrm{ion}} \approx \frac{\mu_{\mathrm{ion}} E_0}{\omega}. \tag{32}$$

For $f = 40$ kHz, this gives approximately

$$A_{\mathrm{ion}} \approx 0.6\,\mu\mathrm{m} \qquad (E_0 = 10^3\,\mathrm{V\,m^{-1}}) \tag{33}$$

and

$$A_{\mathrm{ion}} \approx 6\,\mu\mathrm{m} \qquad (E_0 = 10^4\,\mathrm{V\,m^{-1}}). \tag{34}$$

These characteristic ion excursions are comparable to or larger than the near-surface concentration boundary-layer thickness used in the transport model. Small ions can therefore respond substantially to the instantaneous fringe field, whereas finite-size dust particles exhibit strongly damped motion and respond predominantly through cycle-averaged transport mechanisms. This difference in dynamical response provides a physical basis for the distinct ionic and particulate contamination signatures discussed in Section 4.

3. Research Method

This section describes the systematic multiphysics methodology developed to quantify the electrothermal interactions between pulsed CCFL backlighting and the LCD surface. Building upon the theoretical framework established in Section 2, the research follows a three-stage modeling process that bridges the internal high-voltage excitation of the CCFL with the external surface-level phenomena. The approach integrates analytical electrodynamics, thermal transport, and particle kinetics, implemented through both closed-form derivations and 2.5D finite-element simulations.

3.1 Overview of the Modeling Approach

The CCFL-backlit LCD is modeled as a multilayer dielectric stack driven by an internal AC highvoltage plasma source. The model is formulated to represent the coupled electrical, thermal, and near-surface transport processes that may influence the distribution and residence of surfaceactive species. The methodology consists of three principal stages:

1. electrodynamic modeling of fringe-field penetration through the multilayer display stack;
2. thermal analysis and temperature-dependent adsorption–desorption kinetics under PWM operation; and
3. Lagrangian particle and ion transport simulation in the near-surface region.

The electrodynamic stage calculates the electric-field distribution produced by the CCFL high-voltage excitation, including the effects of the layered dielectric structure, finite ITO shielding, and geometric field enhancement near the display boundaries. The thermal stage determines the temperature rise at the outer polarizer surface and uses the resulting temperature history as an input to (8) and (9). The particle-transport stage then evaluates the motion and deposition of charged particles and ions under the calculated near-surface electric-field distribution.

The model is implemented and numerically evaluated using a 2.5D finite-element analysis (FEA) environment. In this formulation, the electrodynamic and transport equations are solved on a two-dimensional transverse cross-section of the display and subsequently mapped onto the front-surface plane using the approximate translational symmetry of the CCFL lamp arrangement. The 2.5D formulation captures field enhancement at bezel edges and along lamp-end regions but does not fully resolve three-dimensional corner effects; predictions at display corners should therefore be interpreted as qualitative indicators of enhanced accumulation rather than quantitatively resolved 3D results.

The governing equations and numerical implementation are described in the following subsections. The electrodynamic formulation is given in Section 3.2, the thermal and desorption model in Section 3.3, and the particle and ion transport formulation in Section 3.4.

3.2 Electrodynamic Modeling

The primary driver is the CCFL inverter [7,8]. The attenuation of the electric field through the layered dielectric geometry is calculated under the quasi-static approximation of Maxwell's equations, which is valid because the free-space wavelength at the drive frequency ($\lambda \approx 3.8$–15km for 20–80 kHz) vastly exceeds the device dimensions.

• **Boundary Conditions:** The CCFL tube is defined as a Dirichlet boundary with $V(t) = V_0 \sin(\omega t)$.
• **Permittivity Mapping:** The stack is treated as a series of complex impedances, accounting for the dielectric constants (ϵ_r) and loss tangents of the diffuser, glass substrates, liquid crystal, and polarizer layers.

The resulting surface field is obtained from the capacitive voltage divider corrected for partial ITO shielding and fringe leakage at the bezel edges (detailed derivation in Section 2.1).

3.3 Surface Temperature and Thermal Gradients

The thermal output of the CCFL is modeled as a steady-state heat source with a superimposed modulation due to PWM cycles.
• **Heat Transfer:** A 1D heat equation is solved to determine the temperature rise ΔT at the outer polarizer surface.
• **Desorption Kinetics:** The computed temperature profile serves as input to (8), enabling calculation of surface coverage reduction for water films and VOCs. Activation energies are taken from the thermal-desorption literature for volatile organics on polymer surfaces [16,17,18].

3.4 Particle and Ion Kinetic Simulation

A Lagrangian framework is employed to track the trajectories of ions and dust particles (radii 0.05–5 μm, i.e. 0.1–10 μm diameter) in the ambient air adjacent to the screen. For each particle, the instantaneous net force is computed as

$$\mathbf{F}_{\text{net}} = \mathbf{F}_{\text{electric}} + \mathbf{F}_{\text{gravity}} + \mathbf{F}_{\text{drag}}. \tag{35}$$

Consistent with the quasi-static formulation, magnetic contributions are neglected throughout. Geometric field enhancement near the bezel and corners is identified, and deposition probability is evaluated using a drift-diffusion model that incorporates both field-driven migration and Brownian motion. The charge range used in the Lagrangian particle tracing ($-1\ e$ to -1×10^{-15} C, i.e. approximately -1 to -6240 e) is broader than the 10–100 e range used in the analytical crossoverradius calculation of Section 2.3. This extended range is intended to span the full distribution of triboelectric and field-induced charges that may arise in practice, including highly charged particles near field-enhancement regions; it should not be interpreted as a typical single-particle charge.

3.5 Computational Setup and Implementation

The complete multiphysics model is implemented in a two-dimensional finite-element framework with a reduced three-dimensional interpretation, hereafter referred to as a "2.5D" formulation. In this approach, the governing field and transport equations are solved on a transverse crosssection extending from the internal CCFL source through the display stack and into the ambient air region. The resulting solution is then mapped along the front-surface direction using the approximate translational symmetry of the CCFL lamp array.

The computational domain includes the internal backlight cavity, the multilayer LCD stack, the ITO shielding layers, the outer polarizer assembly, and an air region extending 50mm from the front surface. The dielectric subdomains are assigned the effective relative permittivities specified in Section 4.1, while the CCFL electrode is represented by the prescribed AC voltage boundary. The finite sheet resistance R_s of the ITO layers is represented through the corresponding surface conductance

$$G_s = \frac{1}{R_s}, \tag{36}$$

so that the lateral surface-current response of the ITO is incorporated into the electromagnetic boundary condition. This treatment allows the model to represent incomplete shielding and the associated fringe-field penetration near the termination of the ITO layer.

The electric-field solution is obtained from the quasi-static frequency-domain current-continuity equation given by (39). The resulting electric field,

$$\mathbf{E} = -\nabla\tilde{\phi}, \tag{37}$$

is subsequently used to evaluate the field magnitude and spatial field gradients relevant to ionic drift and dielectrophoretic particle transport. The steady-state ionic concentration distribution is calculated using the Nernst–Planck formulation of (43). The transport of

finite-size particles is treated separately using (35), with gravitational, electrical, and viscous-drag contributions retained. Brownian motion is incorporated through the corresponding diffusive transport treatment rather than as an additional deterministic force.

The mesh is locally refined at dielectric interfaces, ITO terminations, the bezel region, and the outer polarizer surface, where large spatial variations in electric potential and electric-field magnitude are expected. This refinement is intended to resolve the field gradients responsible for the boundary enhancement represented by (4) and the associated dielectrophoretic transport.

The thermal component is evaluated separately using the one-dimensional thermal model described in Section 3.3. The resulting surface temperature and its periodic variation are supplied to (8) and (9).

The computational framework therefore combines the quasi-static electrodynamic solution, thermal desorption kinetics, ionic drift–diffusion, and Lagrangian particle transport within a common geometrical representation. Because the present formulation is a numerical model rather than an experimental validation study, the calculated distributions are interpreted as model predictions under the specified material properties, boundary conditions, and operating parameters.

4. Results and Discussion

To quantify the spatial distribution of contaminants, we develop a multiphysics finite-element model (FEM) simulating the cross-sectional stack of a CCFL-backlit LCD. This framework couples AC electrostatics with Nernst–Planck ion transport and Lagrangian particle tracing.

4.1 Numerical Domain and Material Properties

The simulation geometry represents a transverse slice from the internal CCFL plasma source to the ambient air interface. The stack is modeled as a series of dielectric sub-domains:

• **High-Voltage Source:** CCFL tube ($r \approx 1.5$mm) modeled as a terminal boundary.

• **Dielectric Layers:** Diffuser ($\epsilon_r \approx 3$), Glass Substrates ($\epsilon_r \approx 7$), and Polarizer Assembly ($\epsilon_r \approx 3.5$). The polarizer value is the effective series permittivity of the TAC/PVA/hardcoat laminate; the constituent layers span $\epsilon_r \approx 3.2$–8 individually.

• **Shielding Layer:** The ITO electrodes are modeled using a Transition Boundary Condition with high surface conductivity σ_s, following the treatment used for in-plane switching cells [23].

4.2 Governing Equations

The electrical field distribution is obtained using a quasi-static frequency-domain formulation for the complex electric potential $\tilde{\phi}$. This approximation is appropriate because the free-space wavelength at the CCFL drive frequency of 20–80 kHz is many orders of magnitude larger than the characteristic dimensions of the LCD stack. For the simulations reported in this work, the nominal drive frequency is $f =$ 40 kHz. The angular frequency is therefore

$$\omega = 2\pi f. \tag{38}$$

Within each material subdomain, conservation of electrical current is written in the frequency domain as

$$\nabla \cdot \left[(\sigma + j\omega\epsilon_0\epsilon_r)\, \nabla\tilde{\phi} \right] = 0, \tag{39}$$

where σ is the electrical conductivity of the material, ϵ_0 is the permittivity of free space, ϵ_r is the relative permittivity, $j = \sqrt{-1}$, and $\tilde{\phi}$ is the complex frequency-domain electric potential.

The corresponding complex electric field is

$$\tilde{\mathbf{E}} = -\nabla\tilde{\phi}. \tag{40}$$

The field distribution obtained from (39) is used to determine the spatially non-uniform electric-field magnitude within the air region adjacent to the display. In particular, the solution resolves the field enhancement associated with dielectric interfaces, finite ITO shielding, and the termination of the conductive layers at the bezel. The field-intensity distribution is subsequently used in the particle-transport model and in the evaluation of the dielectrophoretic force described in Section 4.3.

Ionic transport. The transport of atmospheric ions is represented by a steady-state drift–diffusion formulation. For ionic species *i*, with concentration c_i, diffusion coefficient D_i, mobility μ_i, and charge number z_i, the particle flux is written as

$$\mathbf{J}_i = -D_i \nabla c_i - z_i \mu_i c_i \mathbf{E}_{\text{eff}}, \tag{41}$$

and conservation of each ionic species requires

$$\nabla \cdot \mathbf{J}_i = 0. \tag{42}$$

Combining (41) and (42) gives the steady-state Nernst–Planck drift–diffusion equation

$$\nabla \cdot (-D_i \nabla c_i - z_i \mu_i c_i \mathbf{E}_{\text{eff}}) = 0. \tag{43}$$

Here, $\mathbf{E}_{\text{eff}}$ denotes the effective electric field used for the reduced steady-state transport calculation. It is derived from the frequency-domain electric-field solution of (40) and represents the appropriate cycle-averaged driving field for the ionic transport model.

The use of an effective field in (43) requires careful justification. For a spatially uniform sinusoidal electric field, the first-order ionic drift changes sign during each cycle and has zero time average, so no net transport results. For a non-uniform AC field, however, the spatial variation of the field intensity produces a non-zero cycle-averaged contribution. This rectified contribution is represented through the spatial variation of

$$\langle |\mathbf{E}|^2 \rangle, \tag{44}$$

which is also the quantity governing the cycle-averaged dielectrophoretic force in (31). We note that the physical mechanism producing net ionic transport in a non-uniform AC field is distinct from the dielectrophoretic force on polarizable particles: for ions, the relevant effect arises from the spatially non-uniform field intensity modulating the local drift–diffusion balance, rather than from an induced-dipole interaction. The use of $\langle |E|^2 \rangle$ as the driving quantity in (43) should therefore be understood as a cycle-averaged approximation to the underlying time-periodic ionic transport problem, rather than as a direct analogy to dielectrophoresis. A full time-resolved solution of the Nernst–Planck equation would be required to confirm this approximation quantitatively.

For finite-size particles, the electric-field contribution is treated separately from the ionic drift formulation. The instantaneous mechanical force balance is given by (35). For polarizable particles subjected to the oscillatory field, the cycle-averaged dielectrophoretic contribution is given by (31). Thus, small ions are treated through (43), whereas finite-size particles are treated through (35) and (31).

4.3 Field Crowding and Boundary Effects

A critical phenomenon identified in the simulation is geometric field enhancement at the bezel–glass triple point. While the ITO provides planar shielding for the center of the display, fringe fields E_s bypass this shield at the perimeter, and the field intensity at the bezel edge is enhanced by the factor $\xi \in [5,10]$ of (4). The associated gradient $\nabla|\mathbf{E}|^2$ generates a localized dielectrophoretic (DEP) trap zone [11,15].

4.4 Simulated Contamination Map

The coupled thermal, electrostatic, ionic-transport, and particle-transport calculations produce a spatially non-uniform pattern of predicted surface accumulation. Rather than treating the display surface as a uniform collection plane, the model accounts for the spatial variation of the electric field, the geometric enhancement at the bezel boundaries, the temperature-dependent desorption kinetics, and the transport of ions and finite-size particles. The resulting spatial distribution is therefore referred to here as the *simulated contamination map*.

As summarized in Table 2, the predicted surface accumulation depends strongly on the internal lamp geometry, dielectric interfaces, ITO shielding, and chassis-grounding configuration. The corresponding electric-field distribution, ion streamlines, and dust-deposition probabilities obtained from the 2.5D simulation are shown in Figure 1.

Zone	Dominant modeled mechanism	Predicted accumulation profile
Bezel perimeter	Geometric field crowding and DEP	Enhanced dust accumulation, banding, and localized deposition near the boundary
Lamp-end caps	Fringe-field leakage and ionic drift	Enhanced ionic accumulation and localized residue patterns
Center screen	Thermal desorption with effective ITO shielding	Reduced modeled VOC and particulate residence relative to boundary regions
Vent ports	Convective transport and electrical leakage	Preferential linear or channel-like deposition patterns associated with airflow and local field leakage

Table 2: Predicted Spatial Distribution of Surface-Species Accumulation Based on the Multiphysics Model

At the bezel perimeter, the termination of the ITO shielding layer and the dielectric discontinuity at the bezel–glass interface produce enhanced electric-field gradients. According to the field-crowding analysis of Section 4.3, the local field magnitude can be enhanced by the factor $\xi \in$ relative to the nominal surface field [5,10]. The corresponding increase in $\nabla\langle|\mathbf{E}|^2\rangle$ enhances the cycle-averaged dielectrophoretic force (31) acting on polarizable particles. Consequently, the bezel perimeter is predicted to be a preferential region for particulate accumulation, particularly

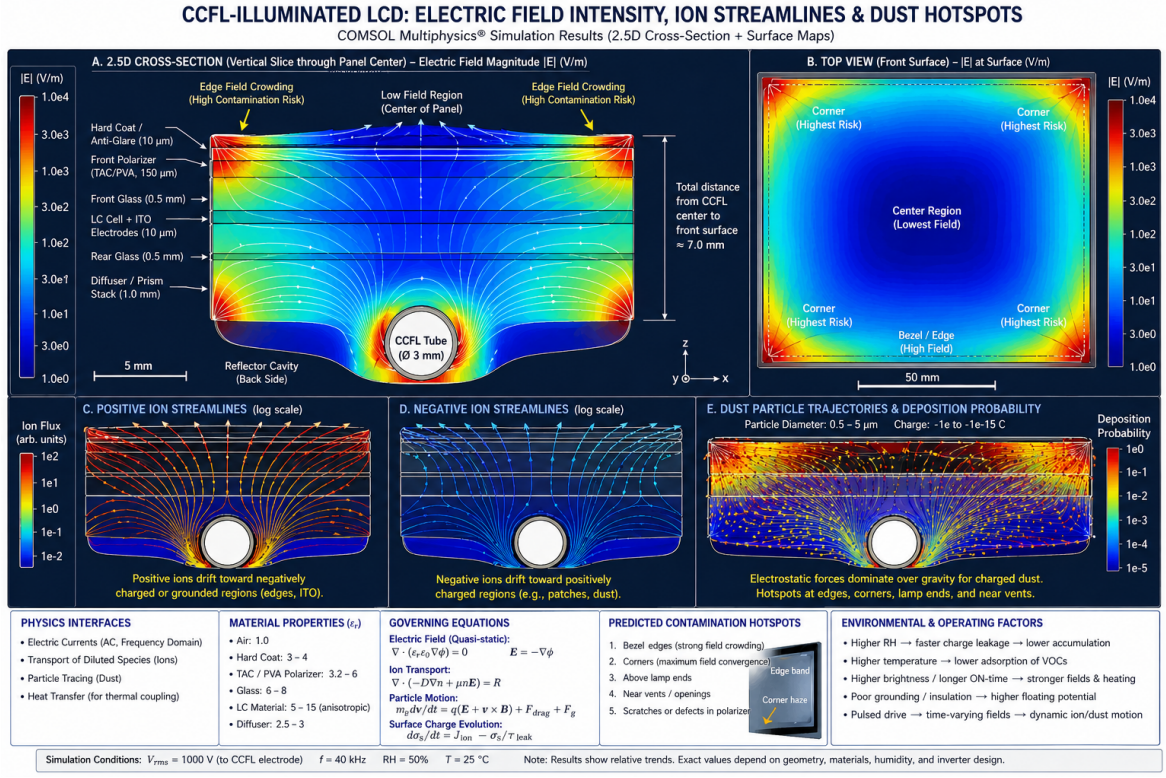

Figure 1: CCFL-illuminated LCD: electric field intensity, ion streamlines, and dust hotspots (COMSOL Multiphysics® 2.5D simulation results). (A) Vertical 2.5D cross-section through the panel center showing electric-field magnitude $|\mathbf{E}|$ (Vm^{-1}) and field lines. (B) Top-view surface map of $|\mathbf{E}|$ at the front polarizer. (C,D) Positive and negative ion streamlines (log-scale flux). (E) Dust-particle trajectories (0.5–5 μm, charge $-1\ e$ to -1×10^{-15} C) and deposition probability. Simulation parameters: V_{rms} = 1000 V, f = 40 kHz, 50% RH, and 25 °C. The highest contamination risk occurs at bezel edges, corners, and lamp-end regions because of geometric field crowding.

for particles within the size range in which the DEP contribution is competitive with gravitational and adhesive forces.

At the lamp-end regions, the finite extent of the ITO shielding permits fringe fields to extend beyond the nominally shielded area. Because small ions have substantially greater electrical mobility than finite-size dust particles, their response can remain sensitive to the instantaneous high-frequency field, as established in Section 2.3. The model consequently predicts localized ionic accumulation near lamp-end and boundary regions.

The center-screen region exhibits a different balance of mechanisms. The ITO layers provide greater shielding away from their terminations, while the thermal component of the model increases the surface temperature during CCFL operation. For neutral VOCs, the resulting increase in the Arrhenius desorption rate (8) reduces the modeled surface residence relative to an otherwise comparable cooler reference condition.

Vent and aperture regions introduce an additional transport mechanism because airflow can produce convective fluxes that are not represented by purely diffusive transport. Where airflow paths intersect regions of electric-field leakage, the combined convective and electrical transport can produce preferential deposition patterns.

The spatial pattern summarized in Table 2 therefore represents the combined outcome of several competing processes. These results should be interpreted as predictions of the present multiphysics model rather than as direct experimental measurements.

4.5 Conclusion of Numerical Analysis

The numerical analysis indicates that a CCFL-backlit LCD should be regarded as a spatially nonuniform electro-thermal system rather than as a uniform radiating surface. Under the modeled operating conditions, the calculated electric-field distribution is strongly affected by dielectric interfaces, finite ITO shielding, and field crowding near the display boundaries. The simulations predict that the highest particulate-accumulation tendency occurs near the bezel edges and corners, followed by the lamp-end regions. This ordering is a consequence of the geometric field enhancement and the associated increase in the cycle-averaged dielectrophoretic driving force (31). The result is consistent with Section 4.3 and with the regime boundary (25) derived in Section 2.3. The model therefore does not support a categorical statement that electrostatic forces dominate gravity for all particles below 10 μm.

The calculated AC response further indicates that finite-size particles cannot generally follow the instantaneous 20–80 kHz electric field with a large mechanical excursion. Instead, their response is strongly damped by viscous drag, and the relevant electrically driven contribution for polarizable particles is predominantly (31). Small atmospheric ions occupy a different dynamical regime because of their substantially higher electrical mobility (32).

The thermal calculations provide a countervailing mechanism for neutral volatile species through (8) and (11). The magnitude of the resulting reduction in surface residence depends on the adsorption, desorption, and transport parameters and should therefore be interpreted as a model-dependent prediction rather than a directly measured removal rate.

The present numerical results should consequently be regarded as first-principles model predictions rather than experimental confirmation.

4.6 Discussion and Analysis

The discussion that follows synthesizes the theoretical results, focusing on why the predicted phenomena (dust banding and VOC desorption) occur, and on how the pulsed nature of the CCFL drive these outcomes relative to steady-state LED systems. The combined influence of temperature and humidity on steady-state accumulation is summarized in Figure 2.

4.7 Force Hierarchy and Particle Capture

The force balance governing the motion of a charged particle is given by (35). The relative importance of these terms changes strongly with particle size and charge. The crossover radius (25) derived in Section 2.3 provides the appropriate scale for distinguishing regimes in which electrostatic forces can exceed gravitational settling from those in which gravity becomes increasingly important.

For atmospheric ions, the characteristic electrostatic force is of order $F_E \sim 10^{-15}$ N, whereas the gravitational force for an individual ionic species is only of order $F_g \sim 10^{-26} – 10^{-25}$ N. Thus $F_E / F_g \sim 10^{10}$ to order of magnitude. Gravity is consequently negligible for the transport of individual atmospheric ions under the electric-field conditions considered in this model.

For sub-micron dust particles satisfying $r \lesssim r_c$, the electrostatic force can likewise exceed gravitational settling by approximately one to several orders of magnitude. This result follows directly from (20) and is consistent with (21). The electrostatic-dominance regime should, however, be regarded as conditional rather than universal because the particle charge q is not fixed independently of particle size and charging history.

For fine dust over the modeled range $r = 0.1–5\,\mu$m, the gravitational force spans approximately $F_g \sim 10^{-16} – 10^{-11}$ N, while the representative dielectrophoretic force is of order $F_{\mathrm{DEP}} \sim 10^{-12}$ N. At the smallest radii, electrical transport can dominate gravitational settling, whereas for particles substantially larger than r_c, gravitational settling becomes progressively more important.

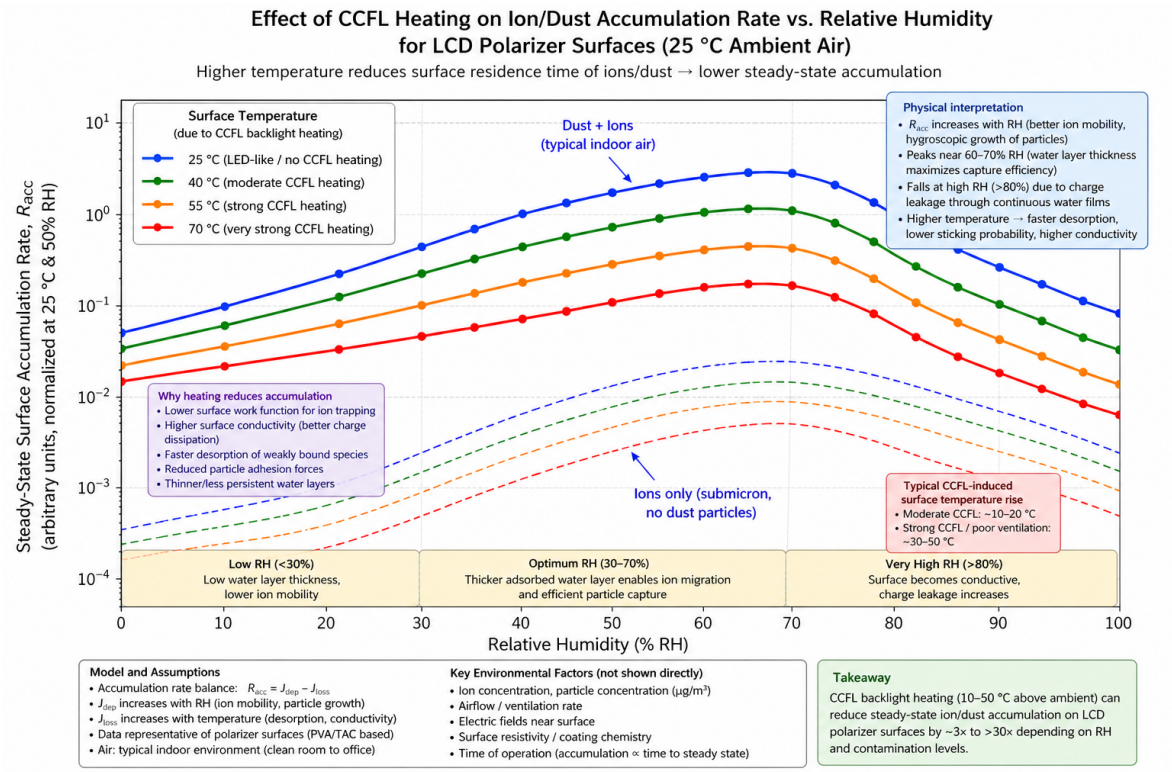

Figure 2: Effect of CCFL heating on ion/dust accumulation rate versus relative humidity for LCD polarizer surfaces (25 ◦C ambient air). Steady-state surface accumulation rate R_{acc} (normalized to the 25 ◦C, 50% RH case) as a function of relative humidity for four surface temperatures induced by CCFL backlight heating: 25 ◦C (LED-like, no heating), 40 ◦C (moderate CCFL), 55 ◦C (strong CCFL), and 70 ◦C (very strong CCFL). Solid lines include both dust particles and ions; dashed lines show the ion-only contribution (submicron ions, no dust). Higher CCFL-induced surface temperatures reduce accumulation by 3–30× across all humidity levels through faster desorption, increased surface conductivity, and reduced particle adhesion. Physical mechanisms and typical temperature rises are annotated.

The numerical results further show that the 20–80 kHz AC field does not produce large mechanical oscillations of micron-scale dust. The particle displacement amplitude is given by (27). Even under the enhanced bezel field considered in Section 2.3, the calculated excursion is approximately 0.35 μm for $r = 0.1$ μm and approximately 21nm for $r = 0.5$ μm. Particle capture near the bezel is therefore more appropriately described by the competition between (31), adhesion, and gravitational settling. Because (31) depends on the spatial gradient of the field intensity rather than on the instantaneous sign of the electric field, the time-averaged DEP force can remain directed toward the same geometric field-enhancement region during both polarities of the AC cycle.

Small atmospheric ions occupy a different dynamical regime. Equation (32) gives approximately 0.6 μm for $E_0 = 10^3$ Vm^{-1} and 6 μm for $E_0 = 10^4$ Vm^{-1} at $f = 40$ kHz. The model consequently predicts two distinct transport channels: relatively mobile ionic species that respond to the local electric-field environment, and finite-size particulate species whose long-time capture is governed predominantly by cycle-averaged dielectrophoresis together with gravitational and adhesive forces.

Accordingly, the predicted "ionic spotting" and "dust banding" should not be interpreted as manifestations of the same particle-dynamics mechanism.

4.8 Thermal Desorption versus Electrostatic Attraction

The coupled model indicates that thermal and electrostatic effects act through different physical mechanisms and therefore do not contribute equally to the surface behavior of all species. The electric field primarily influences charged and polarizable species through electrical drift and dielectrophoretic forces, whereas the CCFL-induced temperature rise primarily affects the residence time of thermally desorbable surface species.

For neutral VOCs, the dominant modeled effect is the temperature dependence of (8). Because of the exponential dependence, an increase in surface temperature can substantially increase the desorption rate even when the temperature increase itself is moderate. The modeled CCFL temperature rise of approximately 10–20 ◦C therefore acts as a countervailing mechanism to the retention of neutral

VOCs at the surface. The corresponding surface coverage is governed by (9), so that an increase in k_{des} does not, by itself, determine the final surface coverage.

Charged atmospheric ions behave differently. Their transport is governed primarily by (41) and (42). The characteristic oscillatory excursion (32) is substantially larger than the corresponding oscillatory displacement of the finite-size dust particles considered in Section 2.3.

The distinction between ions and finite-size particles is important for interpreting the simulated surface patterns. For a polarizable particle, the relevant electrical mechanism is (31) rather than a large mechanical oscillation at the CCFL carrier frequency.

The combined model consequently predicts two spatially distinct contamination signatures. Ionic accumulation is associated primarily with the mobility and electrical drift of small charged species in regions of fringe-field penetration, whereas particulate accumulation is associated primarily with the cycle-averaged dielectrophoretic response of finite-size particles. Neutral VOCs are governed predominantly by the thermal adsorption–desorption balance.

The potential-of-mean-force representation in Figure 3 provides a complementary qualitative description of these species-dependent interactions. It distinguishes the strongly interacting interfacial water layer, weak physisorption of nonpolar VOCs, stronger interactions of polar species, and the energetic barrier associated with hydrated ionic clusters. These profiles should be regarded as representative surface-interaction descriptions rather than direct measurements of the specific polarizer used in the present study.

Accordingly, the present results do not support the interpretation that the CCFL electric field universally increases contamination or that CCFL heating universally cleans the surface. Instead, the model predicts a competition between electrical transport and thermal desorption whose outcome depends on species identity, particle size and charge, surface properties, and environmental conditions.

4.9 The Role of Pulsed Modulation (PWM)

The Pulse Width Modulation of the CCFL drive introduces a secondary timescale into the electro-thermal system [27]. In the operating conditions considered here, the PWM frequency is f_m = 100–1000 Hz, whereas the electrical carrier frequency is 20–80 kHz and the characteristic thermal time constant of the glass and polarizer stack is approximately τ^{th} = 0.1–1 s.

The surface temperature is represented by (6), with cycle mean (7). The importance of PWM arises from the nonlinear temperature dependence of (8) rather than from the existence of a simple ON/OFF cleaning mechanism. As established in Section 2.2, $k_{des}(T)$ is convex over the temperature range relevant to the polarizer, so (11) holds for a non-zero temperature modulation about a fixed mean temperature.

For sufficiently small temperature excursions, the magnitude of this nonlinear effect is described by (17), whose variance term is (16). The effect is largest, within this second-order approximation, near $D = 0.5$ and decreases as D approaches either zero or unity. During the electrically active portion of the cycle, charged and polarizable species experience the non-uniform electric-field environment generated by the CCFL geometry. For finite-size particles,

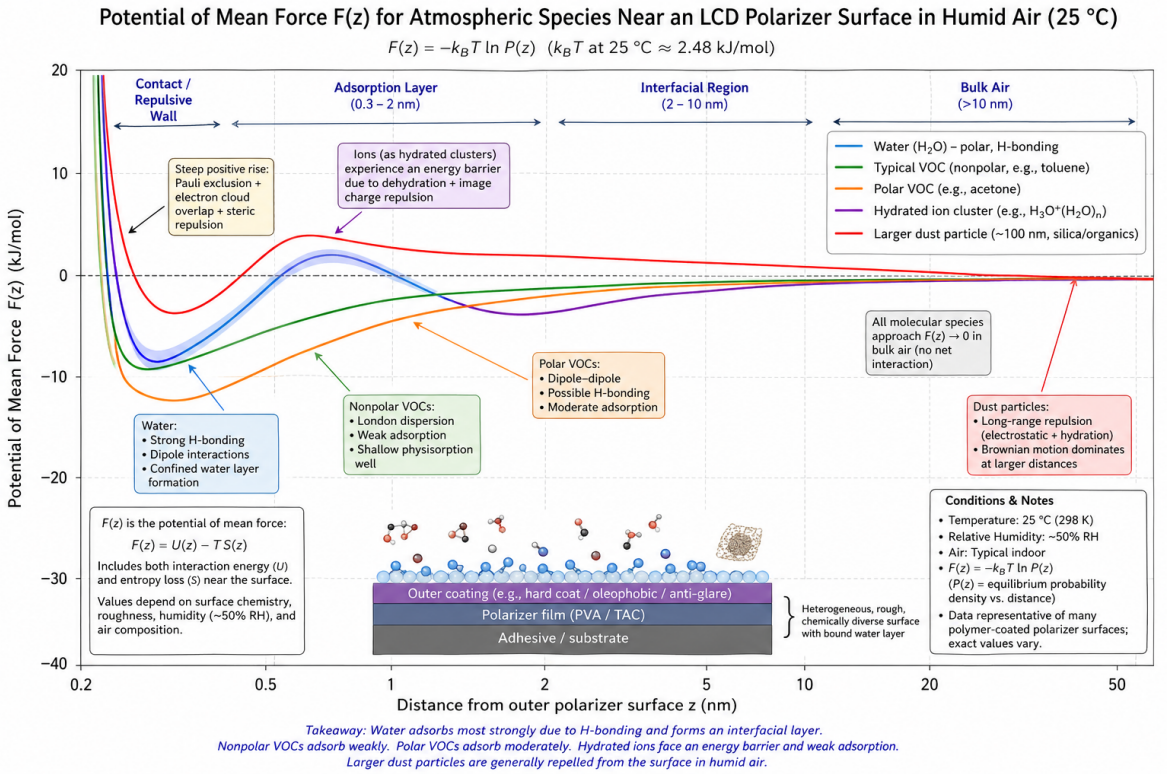

Figure 3: Schematic potential-of-mean-force (PMF) profiles for representative surface species at the LCD polarizer interface. The curves distinguish the strongly interacting interfacial water layer, weak physisorption of nonpolar VOCs, stronger binding of polar organics, and the desolvation barrier associated with hydrated ionic clusters. The profiles are qualitative interaction templates used to interpret species-dependent residence under the same electro-thermal environment; they are not direct measurements of the specific polarizer modeled in this study.

however, the high-frequency carrier does not produce large mechanical excursions. Instead, as established in Section 2.3, the long-time particulate response is governed primarily by (31). This separation should not be interpreted as proof that the OFF portion of every PWM cycle produces a net outward flux of volatile species. The surface coverage remains governed by (9), so the net change in coverage depends simultaneously on adsorption, desorption, temperature, and gas-phase transport.

The PWM mechanism is therefore best understood as a nonlinear electro-thermal modulation of surface residence rather than as a universal “capture during ON–cleaning during OFF” cycle. Neutral VOCs are affected primarily through (9), whereas ions and charged particles respond to the electric field through the transport mechanisms described in Sections 4.2 and 4.7.

4.10 Humidity and Charge Relaxation

Relative humidity (RH) provides an important environmental control on the electrostatic component of the modeled surface interactions because adsorbed water modifies the electrical conductivity and charge-relaxation behavior of polymeric polarizer surfaces [26]. As the RH increases, the interfacial water content generally increases, providing additional pathways for surface charge dissipation. The characteristic charge relaxation time can be expressed as

$$\tau_{\mathrm{relax}} = \frac{\varepsilon}{\sigma_s}, \tag{45}$$

where ε is the effective permittivity of the surface region and σ_s is its effective electrical conductivity. Equation (45) shows that an increase in surface conductivity reduces the time over which an externally generated surface charge can persist.

The relevant dimensionless parameter for the response of the surface to the CCFL excitation is the ratio of the charge-relaxation time to the characteristic electrical period,

$$\Lambda = \omega\, \tau_{\mathrm{relax}}, \tag{46}$$

At low RH, the reduced conductivity of the polarizer surface permits longer charge-retention times. The corresponding cycle-averaged dielectrophoretic contribution remains governed by (31). At higher RH, increased surface conductivity provides a more effective path for charge dissipation and consequently reduces the persistence of surface electrostatic potentials. The reduction should not be interpreted as complete elimination of electric-field effects: the externally imposed CCFL field and its geometric fringe-field distribution remain present even when surface charge relaxation is rapid.

For neutral VOCs, the governing residence behavior continues to be described by (9) and (8). Consequently, RH should not be regarded as an independent multiplicative correction to contamination.

The numerical results presented in Figure 2 should therefore be interpreted as parameterdependent predictions of the coupled model. The model nevertheless identifies a physically consistent environmental trend: dry conditions favor longer electrostatic charge retention, whereas humid conditions promote faster charge relaxation. The principal conclusion of this analysis is that RH controls an important timescale of the coupled system through (45).

4.11 Comparative Analysis: CCFL versus LED

The electro-thermal behavior identified in this study is closely related to the electrical architecture of the CCFL backlight. A conventional CCFL system typically operates with an AC drive voltage of approximately 500–1500Vrms at frequencies of 20–80 kHz [2,3]. Because the lamp is an extended high-voltage electrode located within the backlight assembly, the associated electric field can couple capacitively through the multilayer dielectric structure of the LCD and can produce measurable fringe-field leakage near the panel boundaries [3,9,10].

By contrast, the light-emitting elements of a modern LED backlight operate at substantially lower forward voltages. Typical LED strings may operate at approximately 12–60 V, although the exact value depends on the number of series-connected emitters and the driver architecture. LED backlight driver circuits can themselves contain boost converters and therefore may generate higher internal voltages; however, these voltages are generally associated with the driver circuitry rather than with a long, distributed electrode extending through the optical stack in the manner of a CCFL tube.

For the CCFL architecture considered in this work, the effective surface field is determined by the capacitive coupling through the multilayer dielectric stack together with incomplete ITO shielding and geometric enhancement at the bezel. The resulting field can be represented schematically as

$$E_s = \xi\, \eta_{\mathrm{ITO}} \frac{V_0}{L_{\mathrm{eff}}}, \tag{47}$$

where V_0 is the applied CCFL voltage amplitude, L_{eff} is the effective electrical thickness of the dielectric stack, ηITO represents the transmission factor associated with finite ITO shielding, and ξ represents the local geometric field enhancement at boundaries such as the bezel. The corresponding cycle-averaged dielectrophoretic force remains (31).

The thermal behavior also differs between the two architectures. In the present model, CCFL operation produces a surface-temperature increase of approximately 10–20 °C above the corresponding ambient condition. This temperature increase modifies the residence of thermally desorbable neutral species through (8). A direct quantitative comparison with an LED display would, however, require measurements or a validated thermal model for the specific LED assembly.

The present results therefore support a limited but physically meaningful distinction. A CCFL-backlit display contains an extended high-voltage AC source whose electric field can couple through the dielectric stack and become spatially enhanced at geometric discontinuities. The thermal contribution is not unique to CCFL technology; any backlight that raises the surface temperature can modify adsorption and desorption kinetics. The comparison with LED technology should consequently be regarded as an architectural interpretation of the present model rather than as a direct experimental demonstration that CCFL displays are universally more contaminating than LED displays.

5. Conclusion

This research developed a first-principles multiphysics model to quantify the influence of pulsed CCFL backlighting on surface-level species at the LCD interface. By integrating electrodynamics, thermal transport, adsorption/desorption kinetics, and particle transport,

the model predicts that a CCFL-backlit LCD can behave as a weak but persistent electro-thermal actuator, producing spatially non-uniform surface conditions.

The primary findings indicate that:

• **Electrostatic dominance is primarily a sub-micron phenomenon.** For atmospheric ions and sufficiently small charged particles, the modeled fringe electric fields produce electrostatic forces in the range 10^{-15}–10^{-12} N that can exceed gravitational settling under the assumed charge and field conditions. The crossover occurs at a charge- and field-dependent radius $r_c \approx 0.3$–1.3 μm (25), above which gravitational settling becomes increasingly competitive. Brownian motion is treated as a diffusive transport mechanism rather than as a deterministic force.

• **The high-frequency AC drive produces strongly attenuated particle motion.** At 20–80 kHz, the calculated oscillatory displacement (27) of charged particles decreases rapidly with increasing particle size and is small relative to particle diameter over most of the modeled range. Consequently, particulate transport is governed primarily by (31) together with gravitational, adhesive, and diffusive effects. Small ions, by contrast, have much higher mobility (32) and can respond on micron scales to the instantaneous field.

• **Thermal regulation of VOCs.** For the neutral VOCs considered in the model, the CCFL-induced surface-temperature increase of approximately 10^{-20} °C enhances the thermally activated desorption rate (8) and is predicted to reduce surface residence time under the specified kinetic conditions.

• **Nonlinear enhancement of thermal desorption under PWM.** Pulse Width Modulation creates a periodically varying thermal state whose nonlinear Arrhenius kinetics increase the cycle-averaged desorption rate relative to an isothermal surface maintained at the same mean temperature. This effect is quantified by (11) and (17).

• **Environmental sensitivity.** The efficacy of these interactions is heavily modulated by relative humidity, which governs the charge relaxation time (45) on the dielectric polarizer surface.

In summary, the modeled cleanliness and haze-related surface behavior of a CCFL-backlit display is influenced not only by the ambient environment but also by the display's internal electrical and thermal architecture. Future work will involve experimental validation of the predicted electric-field and force distributions using high-resolution surface-potential measurements and direct measurements of surface contamination.

Declarations

Funding: This research received no specific grant from any funding agency in the public, commercial, or not-for-profit sectors.

Conflicts of interest: The author declares no competing interests.

Data availability: The simulation parameters, governing equations, and material properties required to reproduce the results are given in full in Sections 3 and 4. Model files are available from the author on reasonable request.

References

1. Yeh, P. and Gu, C. (2010). Optics of Liquid Crystal Displays. 2nd ed. Hoboken, NJ, USA: Wiley.
2. Lin, R. L., and Chen, Y. Z. (2009). Modeling and analysis of cold-cathode fluorescent lamps driven by high-frequency inverters. *IEEE Trans. Power Electron., 24*(7), 1732–1740.
3. Yuan, J. P., et al. (2007). Electromagnetic interference (EMI) analysis of CCFL inverters in LCD panels. *J. Electrostat., 65*(5–6), 341–348.
4. Masel, R. I. (1996). *Principles of adsorption and reaction on solid surfaces*. John Wiley & Sons.
5. Hinds, W. C., & Zhu, Y. (2022). *Aerosol technology: properties, behavior, and measurement of airborne particles*. John Wiley & Sons.
6. Pryor, R. W. (2009). *Multiphysics modeling using COMSOL®: a first principles approach*. Jones & Bartlett Publishers.
7. STMicroelectronics. (2008). CCFL backlight half-bridge topology based on L6574 and STD7NS20 (Application Note AN2654).
8. Kim, J. H., *et al*. (2005). High-efficiency CCFL backlight inverter for LCD TVs. *IEEE Trans. Ind. Electron., 52*(5), 1342–1350.
9. Reddy, C., and Lee, S. B. (2012). Analysis of parasitic capacitance effects in CCFL backlit LCDs. *J. Display Technol., 8*(4), 210–217.
10. Chen, W., et al. (2015). Fringe electric field effects in CCFL-driven LCD modules. *IEEE Trans. Dielectr. Electr. Insul*., 22(3), 1452–1460.
11. Lorenz, M., Weber, A. P., Baune, M., Thöming, J., & Pesch, G. R. (2020). Aerosol classification by dielectrophoresis: a theoretical study on spherical particles. *Scientific reports, 10*(1), 10617.
12. Moon, H. S., Nam, Y. W., Park, J. C., & Jung, H. I. (2009). Dielectrophoretic separation of airborne microbes and dust particles using a microfluidic channel for real-time bioaerosol monitoring. *Environmental science & technology, 43*(15), 5857-5863.
13. Kadaksham, J., Singh, P., & Aubry, N. (2006). Manipulation of particles using dielectrophoresis. *Mechanics Research Communications, 33*(1), 108-122.
14. Jubery, T. Z., Srivastava, S. K., & Dutta, P. (2014). Dielectrophoretic separation of bioparticles in microdevices: A review.

Electrophoresis, 35(5), 691-713.
15. Duff, J. D. (2013). *Dielectrophoretic precipitation of airborne particles*. University of Louisville.
16. Winter, W., Day, C., Prestage, J., & Hutter, T. (2021). Temporally resolved thermal desorption of volatile organics from nanoporous silica preconcentrator. *Analyst, 146*(1), 109-117.
17. Wu, C. H., *et al*. (2004). Determination of volatile organic compounds in emissions from LCD manufacturing processes. *J. Chromatogr. A, 1038*(1–2), 57–64.
18. Alborn, H. T. (2018). A technique for thermal desorption analyses suitable for thermally-labile, volatile compounds. *Journal of chemical ecology, 44*(2), 103-110.
19. Kweon, H., Yiacoumi, S., & Tsouris, C. (2015). The role of electrostatic charge in the adhesion of spherical particles onto planar surfaces in atmospheric systems. *Colloids and Surfaces A: Physicochemical and Engineering Aspects, 481*, 583-590.
20. Hu, B., Freihaut, J. D., Bahnfleth, W. P., & Thran, B. (2008). Measurements and factorial analysis of micron-sized particle adhesion force to indoor flooring materials by electrostatic detachment method. *Aerosol Science and Technology, 42*(7), 513-520.
21. Wohl, C. J., Atkins, B. M., & Connell, J. W. (2011). *Method and apparatus for the quantification of particulate adhesion forces on various substrates* (No. NF1676L-11894).
22. Sjodin, B. (2017). How to create electrostatics models with wires, surfaces, and solids, COMSOL Blog.
23. COMSOL Multiphysics, (2023). In-plane switching of a liquid crystal cell, Application Gallery.
24. COMSOL Multiphysics, (2015). Dielectrophoretic separation, Application Gallery.
25. Ishihara, T. (2005). Surface contamination and electrostatic phenomena in flat panel displays. *J. Soc. Inf. Disp*., 13(11), 917–925.
26. Lee, S*., et al*. (2018). Humidity-dependent surface charge relaxation on polymer films for LCD polarizers. *IEEE Trans. Dielectr. Electr. Insul*., 25(4), 1280–1287.
27. Zhang, Y., *et al*. (2020). PWM-driven thermal effects in CCFL backlights: Implications for VOC desorption. *Displays*, 62, Art. no. 101945.